Engineering Science and Technology, an International Journal 57 (2024) 101810

Contents lists available at ScienceDirect

Engineering Science and Technology, an International Journal

journal homepage: www.elsevier.com/locate/jestch

Full Length Article

Broadband asymmetric absorption-transmission and double-band rasorber of electromagnetic waves based on superconductor ceramics metastructures-photonic crystals

Lei Lei, Bao-Fei Wan, Si-Yuan Liao, Hai-Feng Zhang *

College of Electronic and Optical Engineering & College of Flexible Electronics (Future Technology), Nanjing University of Posts and Telecommunications, Nanjing, 210023, China

ARTICLE INFO

Keywords:
Superconductor ceramics
Metastructure-photonic crystals
Broadband asymmetric absorption-transmission
Quasi-periodic cascading structure
Rasorber

ABSTRACT

In this paper, a kind of superconductor ceramics metastructure-photonic crystals (SCMPC) is proposed to investigate the absorption and transmission properties of electromagnetic waves (EW) by combining a metastructure with multiple degrees of freedom regulation and strong energy localization characteristics of photonic crystals. Firstly, for the periodically aligned SCMPC, EW mainly realizes absorption in forward propagation and transmission in backward case. The relative bandwidth (*RB*) for both forward absorptivity and backward transmittance greater than 0.9 is 2.7 %, and the operating bandwidth (*OB*) is 696 ~ 715 terahertz (THz), which is an asymmetric absorption-transmission (AAT) characteristics. Importantly, the periodically aligned SCMPC can realize the double-band rasorber phenomenon, and the forward EW exhibits an absorption-transmission-absorption phenomenon with *OBs* of 644.2 ~ 671.1 THz, 700.9 ~ 742.1 THz, and 766.8 ~ 784.2 THz. *RBs* with absorption and transmissivity greater than 0.8 are 4.1 %, 5.7 %, and 2.2 %, respectively, and the backward EW one is mainly transmitted. To optimize AAT, a quasi-periodic Octonacci sequence-aligned SCMPC is introduced. The results show that the maximum *OB* of forward absorption and backward transmission is 428.3 ~ 670.5 THz and *RB* is 44.1 %, achieving favorable broadband AAT. In addition, the effects of temperatures, dielectric thicknesses, and stacking numbers on AAT are also investigated in detail. In conclusion, AAT has promising applications in unidirectional optical transmission, photodiodes, optical isolators, etc.

1. Introduction

Asymmetric propagation of electromagnetic waves (EW) refers to the medium exhibiting different transmission characteristics of EW along various propagation directions, including transmission, reflection, absorption, and polarization conversion [1–3]. This asymmetric property has potential applications in optical communications [4,5], information processing [6,7], and integrated photonic systems for all-optical computing [8,9], which can realize a variety of irreversible electromagnetic devices, such as isolators [10], radomes [11], and circulators [12,13]. The traditional method to realize asymmetric property involves utilizing Faraday magneto-optical effects to break the time-reversal symmetry and achieve unidirectional propagation of EW [14–18]. However, these effects require an applied magnetic field bias, leading to the disadvantages of large device size and integration complexity [19]. In 2006, Fedotov *et al.* [20] first proposed irreversible devices for EW without applied magnetic field bias, which is generated as a result of the interaction of EW with planar chiral structures on subwavelength scales, and this finding has attracted increasing attention. At present, most asymmetric devices operate in low-frequency bands, such as microwave [21] and terahertz (THz) bands [8], while there are fewer studies on asymmetric devices in visible light bands [15]. In 2016, Tang *et al.* [4] proposed a broadband asymmetric transmission device that can achieve a high transmission contrast at visible frequencies by combining a transparent substrate (sapphire) with a tapered metal grating. The device achieves transmission efficiencies of 95 % and 35 % for forward irradiation and backward irradiation, respectively, and the corresponding transmission ratio is greater than 2.5 %. However, it is still a challenge to design asymmetric devices with simple structures that can achieve both absorption and transmission characteristics at visible

* Corresponding author at: College of Electronic and Optical Engineering & College of Flexible Electronics (Future Technology), Nanjing University of Posts and Telecommunications, Nanjing, 210023, China.

E-mail addresses: hanlor@njupt.edu.cn, hanlor@163.com (H.-F. Zhang).

https://doi.org/10.1016/j.jestch.2024.101810
Received 3 May 2024; Received in revised form 10 July 2024; Accepted 9 August 2024
Available online 17 August 2024

frequencies, which can be applied in the fields of communications [22,23], optical devices [24,25], and antennas [26].

In addition, the frequency selection rasorbers [27], which possess the unique property of being transparent to incident EW within the passband while absorbing them outside the passband, have aroused the interest of researchers in recent years. It transmits signals at the operating frequency and can also act as an absorber outside the passband to reduce mutual interference between different communication systems [28], thus achieving stealth. In 2020, Jia *et al.* [29] proposed a selection rasorber with independently controlled dual-frequency transmission response with a lossy layer consisting of four square rings and two short-cuts, and the two frequencies can be individually controlled by changing the lengths of the two short-cuts separately. In the same year, Wu *et al.* [30] designed a low-loss frequency selection rasorber based on an omnidirectional planar graphene sheet resistor with a low-loss single-channel transmission window above the absorption band. However, so far, the research on frequency selection rasorbers is mostly limited to single frequency channels or single frequency points, and there are only a few studies based on double-band rasorbers. Therefore, designing rasorbers with the double-band has been one of the important research topics of great interest.

Superconductor ceramics (SC) are a group of ceramics that exhibit zero electrical resistance and completely repel magnetic fields at critical temperatures [31]. In addition, when the external environment is below the critical current and critical magnetic field, SC exhibits zero resistivity and zero magnetic induction [31]. Superconductivity was first discovered in mercury in 1911 [32], and SC has the advantages of low loss, low dispersion, and wide bandwidth compared to conventional metals [33]. Therefore, SC can be used in various fields, including electric power systems and transportation [33]. Moreover, since the refractive index of SC depends on the London penetration depth, which is related to temperature, it is possible to change the refractive index of SC by altering its temperature [3435]. In 2019, Aly *et al.* [36] proposed a novel one-dimensional defected photonic crystal composed of metamaterial and high T_C SC called Hg1223, which can be used to obtain tunable filtering properties by varying the thicknesses of the metamaterial and SC layers. In 2019, Trabelsi *et al.* [37] designed a quasi-photonic structure made of Yttrium Barium Copper Oxide (YBCO) SC and SiO_2 dielectric materials that can manipulate the position of the transmission peaks and the width of the subphotonic bandgap by optimizing the operating temperature of SC, and the thickness of the layers. Although there are many reports on SC, few studies have combined SC with the asymmetric propagation properties of EW.

Metastructures are artificial composite materials with extraordinary physical properties that cannot be found in natural materials, such as negative refractive index [38], negative dielectric constant [39], and anti-Doppler effect [40]. Through the specific design of metastructures, it is possible to regulate the propagation direction and amplitude of EW, which is conducive to the integration and miniaturization of optical devices. Photonic crystals are artificial periodic multilayer media consisting of two or more materials with different refractive indices alternately [41,42], which have attracted much attention because of the excellent control of EW. Quasi-periodic photonic crystals are characterized by periodicity and randomness, and their peculiar optical properties have attracted great interest in the past decades [43]. Photonic crystals show unique advantages in energy localization and are more likely to form broadband structures. However, they have limited tunable degrees of freedom and weak anisotropy. Metastructures, on the other hand, are generally more suitable for designing anisotropic devices with structures that exhibit strong asymmetric propagation properties but have insufficient operational bandwidth. To address the drawbacks of each, metastructures and photonic crystals are combined to form metastructures-photonic crystals, a distinct class of photonic crystals. Metastructures-photonic crystals allow the design and adjustment of the shape, size, and arrangement of metastructures to regulate and optimize the properties of photonic crystals, thereby achieving specific optical properties and applications.

In this paper, a kind of superconductor ceramics metastructure-photonic crystals (SCMPC) is proposed to investigate the propagation properties of EW. The results demonstrate that the periodically aligned SCMPC can achieve asymmetric absorption-transmission (AAT) of EW at 696 ~ 715 THz and exhibit the double-band rasorber phenomenon. Specifically, the forward-incident EW presents absorption-transmission-absorption characteristics at *OBs* of 644.2 ~ 671.1 THz, 700.9 ~ 742.1 THz, and 766.8 ~ 784.2 THz, respectively, corresponding to absorption above 0.8 with *RBs* of 4.1 %, 5.7 % and 2.2 %. With the introduction of quasi-periodic Octonacci sequences, the SCMPC offers enhanced capabilities in achieving broadband AAT. In the frequency range of 428.3 to 670.5 THz, the *RB* with absorption greater than 0.9 reaches 44.1 %. The results in this paper provide possibilities for designing AAT-based optical devices in broadband-like diodes.

2. Structure design and numerical method

Fig. 1(a) presents a three-dimensional view of the SCMPC, where the SCMPC is infinitely extended in the *y*-direction. The schematic of the periodically aligned SCMPC is illustrated in Fig. 1(b), where two coordinate systems are defined, the original: (x, y, z) and the one with a certain inclination angle: (x', y', z'). The EW is incident on the *xoz* plane at an incidence angle θ. The direction of the magnetic field of transverse magnetic (TM) modes [44] is perpendicular to the plane of the propagation direction, and the directions of forward propagation (along the $-z$-axis) and backward case (along the $+z$-axis) are indicated by arrows. The thicknesses of the metal layer A and SC layer B are described as d_a and d_b, the inclination angle of the SCMPC 1 with respect to the $+z$-axis is φ, and the ambient temperature is fixed to be $T_0 = 50$ K. Details of other parameters involved in the SCMPC 1 are shown in Table 1. The fabrication of the SCMPC is illustrated in Section 1 of Supplementary Material.

For the high-temperature SC ($YaBa_2Cu_3O_7$) with a refractive index $n_D = \sqrt{\varepsilon_D}$, the dielectric function ε_D is described by the two-fluid model and the London local electrodynamics [34]. When the temperature is below the critical temperature [35], the $YaBa_2Cu_3O_7$ ceramic material can be considered a lossless medium. The dielectric function of $YaBa_2Cu_3O_7$ ceramic material is described by the following model [45]:

$$\varepsilon_D = 1 \frac{1}{\omega^2 \mu_0 \varepsilon_0 \lambda_L(T)^2} \tag{1}$$

where ε_0, μ_0 are the free-space permittivity and magnetic permeability, and $\lambda_L(T)$ is the temperature-dependent London penetration length given by [45]:

$$\lambda_L(T) = \frac{\lambda_L(0)}{\sqrt{1 - \left(\frac{T}{T_C}\right)^P}} \tag{2}$$

In Eq. (2), $\lambda_L(0)$ is the London penetration length at T=0 K, P=4, and T_C is the SC critical temperature. In this paper, the $YaBa_2Cu_3O_7$ ceramic material has T_C=92 K, P=4, and λ_L (0) is determined to be 200 nm [34].

Furthermore, the dielectric constant of silver is described by the Drude model [46,47]:

$$\varepsilon_M = 1 - \frac{\omega_P^2}{\omega^2 + i\gamma\omega} \tag{3}$$

where ω_P is the bulk plasma frequency, and γ is the damping constant describing the loss. In this paper, we choose metallic silver, which is known to have the following relevant parameters according to the study [9] which are μ_M=1, ω_P=1.2 × 10^{16} rad/s, $\gamma = 1.0 \times 10^{14}$ rad/s.

In the coordinate system $x'y'z'$, the effective relative permittivity tensor (Maxwell-Garnett homogenization) of the periodically aligned SCMPC is [9]:

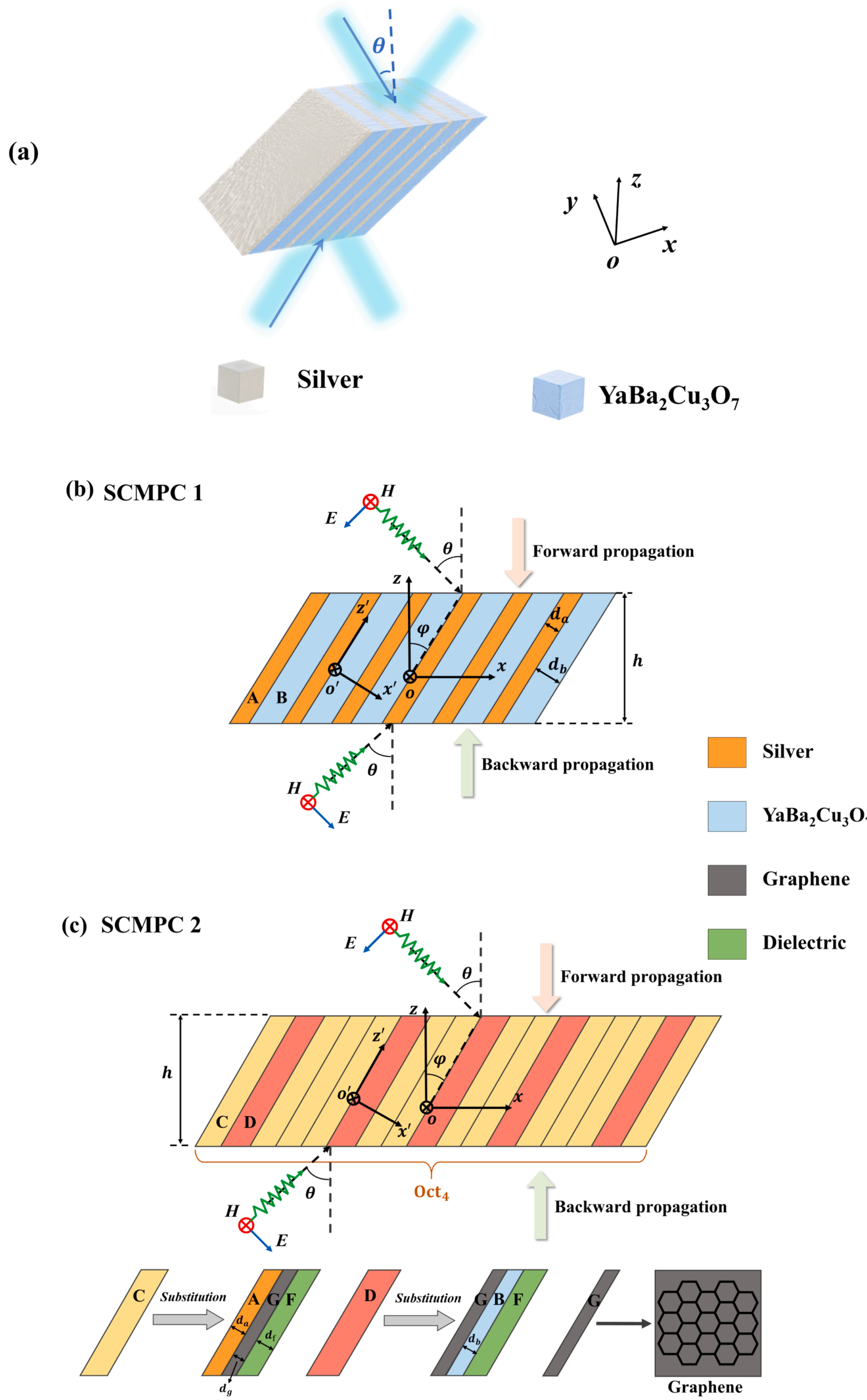

Fig. 1. (a) Structural three-dimensional view of the SCMPC. (b) Schematic representation of the periodically aligned SCMPC. (c) Schematic representation of the quasi-periodic Octonacci sequence-aligned SCMPC. Layer A denotes the metal, layer B denotes the SC, and θ denotes the angle of incidence. The $x'y'z'$ axis is obtained by rotating the xyz axis about the y' axis by an angle φ. The two opposing arrows at the top and bottom outside the SCMPC indicate EW incident in the forward and backward directions, respectively. The substitution rules for the colored blocks are plotted in detail.

Table 1
Parameters of two SCMPCs realizing different functions.

AAT of the SCMPC 1						
d_a (nm)	d_b (nm)	h (nm)	φ (°)	θ (°)		
9	12	102	30	50		
Double-band rasorber of the SCMPC 1						
d_a (nm)	d_b (nm)	h (nm)	φ (°)	θ (°)		
8.4	26	43	45	60		
Broadband AAT of the SCMPC 2						
d_a (nm)	d_b (nm)	d_f (nm)	d_g (nm)	h (nm)	φ (°)	θ (°)
4	12	15	3.4	90	40	45

$$\overline{\varepsilon}' = \begin{bmatrix} \varepsilon'_{xx} & 0 & 0 \\ 0 & \varepsilon'_{yy} & 0 \\ 0 & 0 & \varepsilon'_{zz} \end{bmatrix} \tag{4}$$

where $\varepsilon'_{xx} = \frac{d_a+d_b}{d_a/\varepsilon_M+d_b/\varepsilon_D}$, $\varepsilon'_{yy} = \varepsilon'_{zz} = \frac{d_a\varepsilon_M+d_b\varepsilon_D}{d_a+d_b}$ [9], ε_M is the dielectric constant of silver and ε_D is the dielectric constant of $YaBa_2Cu_3O_7$ ceramic material.

So, in the coordinate system $x'y'z'$, the electric field vector $\boldsymbol{D}'$ and electric filed vector $\boldsymbol{E}'$ can be described as [9]:

$$\boldsymbol{D}' = \varepsilon_0\overline{\varepsilon}'\boldsymbol{E}' \tag{5}$$

In addition, the coordinate system xyz and the coordinate system $x'y'z'$ are related as follows [9]:

$$\begin{bmatrix} x \\ y \\ z \end{bmatrix} = \begin{bmatrix} \cos\varphi & 0 & \sin\varphi \\ 0 & 1 & 0 \\ -\sin\varphi & 0 & \cos\varphi \end{bmatrix} \begin{bmatrix} x' \\ y' \\ z' \end{bmatrix} = \boldsymbol{R} \begin{bmatrix} x' \\ y' \\ z' \end{bmatrix} \tag{6}$$

where φ is the inclination of the SCMPC with respect to the + z axis, $\boldsymbol{R} = \begin{bmatrix} \cos\varphi & 0 & \sin\varphi \\ 0 & 1 & 0 \\ -\sin\varphi & 0 & \cos\varphi \end{bmatrix}$.

Furthermore, in the coordinate system xyz, the electric displace vector $\boldsymbol{D}$ and electric filed vector $\boldsymbol{E}$ can be described as [9]:

$$\boldsymbol{D} = \varepsilon_0\varepsilon\boldsymbol{E} \tag{7}$$

In the coordinate system xyz, the effective relative permittivity tensor of the periodically aligned SCMPC is transformed into [9]:

$$\varepsilon = \begin{bmatrix} \varepsilon_{xx} & 0 & \varepsilon_{xz} \\ 0 & \varepsilon_{yy} & 0 \\ \varepsilon_{zx} & 0 & \varepsilon_{zz} \end{bmatrix} \tag{8}$$

where, ε_{xx}, ε_{yy}, ε_{zz}, ε_{xz}, ε_{zx} can be represented as [9]:

$$\begin{aligned} \varepsilon_{xx} &= \varepsilon'_{xx}\cos^2\varphi + \varepsilon'_{yy}\sin^2\varphi \\ \varepsilon_{zz} &= \varepsilon'_{xx}\sin^2\varphi + \varepsilon'_{yy}\cos^2\varphi \\ \varepsilon_{xz} = \varepsilon_{zx} &= \left(\varepsilon'_{yy} - \varepsilon'_{xx}\right)\sin\varphi\cos\varphi \end{aligned} \tag{9}$$

When a plane EW is incident on the SCMPC, the two wave vectors of the two waves incident forward ($-z$-direction) and backward ($+z$-direction) with respect to the boundary are very different due to the presence of a tilted optical axis and a non-zero incidence angle [9]. Next, we proceed based on source-free Maxwell of Eq.(9). First, the magnetic field has only y-directional components for both forward and backward incidence of the TM wave, so the magnetic field can be represented as [9]:

$$\boldsymbol{H}_y = \boldsymbol{H}_y^+\overrightarrow{y} + \boldsymbol{H}_y^-\overrightarrow{y} = \boldsymbol{H}_{y_0}^+ e^{i\left(k_z^+ z + k_x x - \omega t\right)}\overrightarrow{y} + \boldsymbol{H}_{y_0}^- e^{i\left(k_z^- z + k_x x - \omega t\right)}\overrightarrow{y} \tag{10}$$

where k_z^+ and k_z^- indicate the $+z$ and $-z$ components of wave vectors, respectively. Thus, we have [9]

$$\nabla \times \boldsymbol{H}_y = \begin{vmatrix} \overrightarrow{x} & \overrightarrow{y} & \overrightarrow{z} \\ \frac{\partial}{\partial x} & \frac{\partial}{\partial y} & \frac{\partial}{\partial z} \\ 0 & H_y & 0 \end{vmatrix} = \left(-ik_z^+H_y^+ - ik_z^-H_y^-\right)\overrightarrow{x} + ik_x\left(H_y^+ + H_y^-\right)\overrightarrow{z} \tag{11}$$

According to Eqs.(7) and (9), we can get [9]

$$\begin{pmatrix} D_x \\ 0 \\ D_z \end{pmatrix} = \varepsilon_0 \begin{pmatrix} \varepsilon_{xx} & 0 & \varepsilon_{xz} \\ 0 & \varepsilon_{yy} & 0 \\ \varepsilon_{zx} & 0 & \varepsilon_{zz} \end{pmatrix} \begin{pmatrix} E_x \\ 0 \\ E_z \end{pmatrix} \tag{12}$$

$$\frac{\partial \boldsymbol{D}}{\partial t} = -i\omega\varepsilon_0(\varepsilon_{xx}E_x + \varepsilon_{xz}E_z)\overrightarrow{x} - i\omega\varepsilon_0(\varepsilon_{zx}E_x + \varepsilon_{zz}E_z)\overrightarrow{z} \tag{13}$$

From $\nabla \times \boldsymbol{H}_y = \frac{\partial \boldsymbol{D}}{\partial t}$, we have [9]

$$\begin{cases} k_z^+H_y^+ + k_z^-H_y^- = \omega\varepsilon_0(\varepsilon_{xx}E_x + \varepsilon_{xz}E_z) \\ k_x\left(H_y^+ + H_y^-\right) = -\omega\varepsilon_0(\varepsilon_{zx}E_x + \varepsilon_{zz}E_z) \end{cases} \tag{14}$$

Then, we derive E_x From Eq.(14), the result is [9]:

$$E_x = \frac{\varepsilon_{zz}k_z^+ + \varepsilon_{xz}k_x}{\omega\varepsilon_0\left(\varepsilon_{xx}\varepsilon_{zz} - \varepsilon_{xz}^2\right)}\boldsymbol{H}_y^+ + \frac{\varepsilon_{zz}k_z^- + \varepsilon_{xz}k_x}{\omega\varepsilon_0\left(\varepsilon_{xx}\varepsilon_{zz} - \varepsilon_{xz}^2\right)}\boldsymbol{H}_y^- \tag{15}$$

for the $+z$ direction plane wave, from $\nabla \times \boldsymbol{E} = -\frac{\partial \boldsymbol{B}}{\partial t}$, we can get [9]

$$\left(\frac{\partial E_x}{\partial z} - \frac{\partial E_z}{\partial x}\right) = i\omega\mu_0\mu H_y^+ \tag{16}$$

$$\varepsilon_{zz}k_z^2 + (\varepsilon_{xz}k_x + k_x\varepsilon_{zx})k_z + \varepsilon_{xx}k_x^2 = k_0^2\left(\varepsilon_{xx}\varepsilon_{zz} - \varepsilon_{xz}^2\right) \tag{17}$$

From Eq.(17), we can get two solutions for k_z, which are as follows [9]:

$$k_z^1 = \frac{\left[-\varepsilon_{xz}k_x + \sqrt{\left(\varepsilon_{xz}^2 - \varepsilon_{zz}\varepsilon_{xx}\right)\left(k_x^2 - k_0^2\varepsilon_{zz}\right)}\right]}{\varepsilon_{zz}} \tag{18}$$

$$k_z^2 = \frac{\left[-\varepsilon_{xz}k_x - \sqrt{\left(\varepsilon_{xz}^2 - \varepsilon_{zz}\varepsilon_{xx}\right)\left(k_x^2 - k_0^2\varepsilon_{zz}\right)}\right]}{\varepsilon_{zz}} \tag{19}$$

where $k_x = k_0\sin\theta, k_0 = \omega/c$ [9]. Additionally, k_z is the normal wave vector component of a plane EW, and its two different solutions k_z^1 and k_z^2 indicate that the plane EW is incident in two different directions which are forward and backward, respectively.

For ordinary materials, k_z^1 and k_x^2 are opposite and the structure can be viewed as reversible [9]. However, in this paper, for the SCMPC 1, when k_x is not equal to 0, k_z^1 and k_z^2 do not have an inverse relationship. Therefore, plane EWs have different propagation processes in forward and backward cases, which is the origin of AAT properties. In addition, the components of the electric field vector on the metal layer are different when the plane wave is incident from different directions. That is, the titled metal layer has different interactions with the electric field vector incident from different directions. For both k_z, the corresponding $+z$ or $-z$-directions depend on the incidence direction and the imaginary part of k_z. When incident in the $+z$-direction, k_z with a positive imaginary part corresponds to a plane wave in the $-z$-direction, and k_z with a negative imaginary part corresponds to a plane wave in the $-z$-direction. Energy coefficients for EW propagation in the SCMPC is illustrated in Section 2 of Supplementary Material.

To optimize AAT performance, a quasi-periodic Octonacci sequence-aligned SCMPC is proposed based on the SCMPC 1, which is displayed in Fig. 1(c). The Octonacci sequence has a relatively symmetric recursive rule [48], which can be expressed as S_M=$S_{M\text{-}1}S_{M\text{-}2}S_{M\text{-}1}$, $M\geq2$, where M represents the stacking numbers, and the initial parameters are S_1={C},

S_0={D}. Thus, S_2={CDC}, S_3={$CDCCCDC$}, and so on can be obtained by the recursive rule [48]. Where the substitution rules are shown in Fig. 1(c), C is replaced with a combination of metal layer A, graphene layer G, and dielectric layer F, and D is replaced with a combination of graphene layer G, SC layer B, and dielectric layer F. In the SCMPC 2, the thicknesses of dielectric layer F and graphene layer G are d_f and d_g, respectively. The dielectric constant of the dielectric layer F is noted as $\varepsilon_f = 1.21$, and the ambient temperature T_0 is fixed as 50 K. Similarly, the other parameters are displayed in Table 1. The dielectric functions for metal and SC have been given by Eqs.(1), (2) and (3).

The conductivity of the graphene can be calculated by the Kubo equation [49]:

$$\sigma_g = \sigma_g^{\text{inter}} + \sigma_g^{\text{intra}} \tag{20}$$

where σ_g^{inter} and σ_g^{intra} are the inter-band and intra-band conductivities of graphene [49].

$$\sigma_g^{\text{intra}} = \frac{ie^2 k_B T_0}{\pi \hbar^2 (\omega + i/\tau)} \left(\frac{\mu}{k_B T_0} + 2\ln(e^{-\frac{\mu}{k_B T_0}} + 1) \right) \tag{21}$$

$$\sigma_g^{\text{inter}} = i\frac{e^2}{4\pi\hbar} \ln\left[\frac{2|\mu| - \hbar(\omega + i/\tau)}{2|\mu| + \hbar(\omega + i/\tau)} \right] \tag{22}$$

where T_0 refers to the ambient temperature, $\mu = 0.1$ eV is the chemical potential, $\tau = 1$ ps is the relaxation time, and k_B is the Boltzmann constant. If the electronic energy band structure of the graphene layer is not affected by the periphery, then its dielectric function can be described as [49]:

$$\varepsilon_g = 1 + i\sigma_g / \omega\varepsilon_0 d_0 \tag{23}$$

In which, ε_0 is the dielectric constant in vacuum and $d_0 = 0.34$ nm indicates the thickness of the monolayer graphene layer [49].

3. Results and discussion

3.1. AAT and double-band rasorber of the SCMPC 1

To investigate the AAT mechanism of the SCMPC 1 more clearly, based on the parameters in Table 1, the changes in the imaginary and real parts of the normal wave vector components k_z^1, k_z^2 concerning the operating frequency are shown in Fig. 2. From Fig. 2(a), the imaginary part of k_z^1 decreases rapidly near the frequency of 790 THz and the minimum occurs at 792 THz, this anomalous dispersion behavior is caused by the current material. In Fig. 2(b), the real part of k_z^1 changes from negative to positive near 800 THz.

Based on the parameters of AAT of the SCMPC 1 in Table 1, the absorption for forward incidence and transmission for backward case are calculated when TM modes are incident in different directions and plotted in Fig. 3(a). Where A denotes absorption, T denotes transmittance. The results show clear AAT phenomena, where TM modes are mainly absorbed at the forward incidence and transmitted at the backward case with an OB of 696 ~ 715 THz and RB of 2.7 %.

In addition, when the parameters of the double-band rasorber of the SCMPC 1 in Table 1 are calculated, the relevant results are illustrated in Fig. 4(a). It can be seen that in the range of 644.2 ~ 671.1 THz and 766.8 ~ 784.2 THz, the forward EW is mainly absorbed, and RBs with absorption greater than 0.8 are 4.1 % and 2.2 %, respectively. In contrast, in the range of 700.9 ~ 742.1 THz, the forward EW is mainly transmitted, and RB with transmission greater than 0.8 is 5.7 %. In general, the absorption-transmission-absorption propagation properties can be achieved at 644.2 ~ 784.2 THz for the forward incidence of plane EWs. The backward EW is still mainly transmitted, and the transmittance of its effective region is higher than 0.9, which can be seen in Fig. 4(b).

From Fig. 5(a), it can be seen that both absorption bands of the forward incident wave maintain high absorption characteristics in the range of 32°~67°. When $\theta = 60°$, the two absorption band regions above 0.8 reach maximum values with OBs of 644.2 ~ 671.1 THz and 766.8 ~ 784.2 THz, and RBs of 4.1 % and 2.2 %, respectively. In Fig. 5(b), for the forward incident EW, the transmission is greater than 0.8 in the range of 0°~75°, which can maintain a certain degree of angular stability.

According to Eq.(1), it is known that the dielectric constant of SC depends on the temperature of the system, and naturally, the absorption and transmission characteristics of EW propagating in different directions are also affected by temperature. Considering that SC can be considered lossless below the critical temperature, four temperatures, T_0 = 5 K, 30 K, 55 K, and 80 K are selected for discussion. In Fig. 6(a) and (b), temperatures have a modulating effect on the double-band rasorber phenomenon. As ambient temperature T_0 increases, RB with forward absorptivity and transmittance higher than 0.8 tends to first increase and then decrease. When T_0 = 5 K, the RBs of the two absorption bands and one transmission band are 4.1 %, 2.3 %, and 6.2 %, respectively. When T_0 = 55 K, the corresponding three RBs are 4.9 %, 4.1 % and 6.7 %. However, as the temperature continues to rise to T_0 = 80 K, all three RBs tend to decrease, corresponding to 2.0 %, 5.7 %, and 3 %.

3.2. Broadband AAT of the SCMPC 2

Fig. 3 shows the difference in absorption and transmission for relative incidence, but the difference is limited and the absorption is not

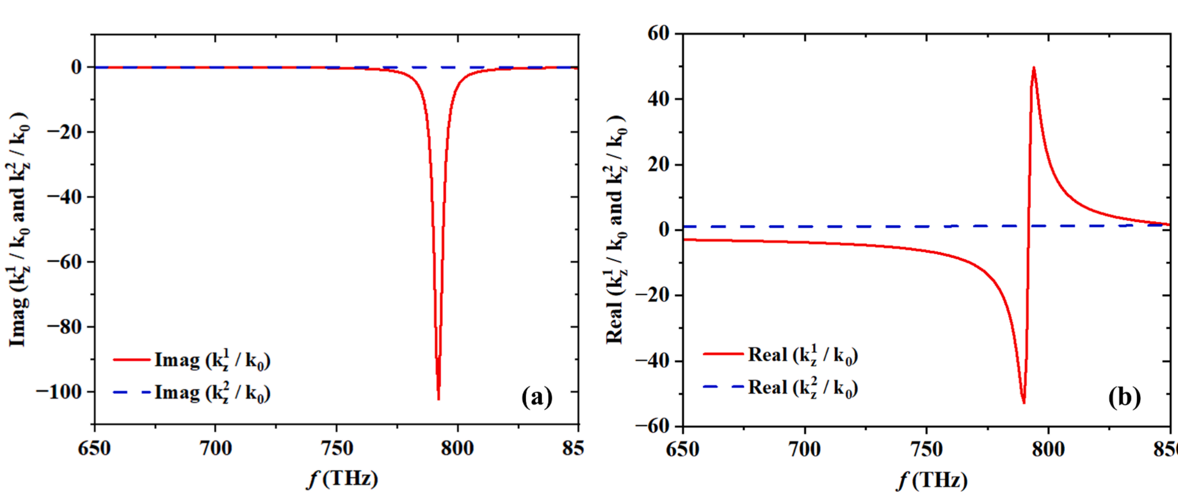

Fig. 2. (a) The imaginary parts and (b)the real parts of of the two plane EWs in SCMPC 1.

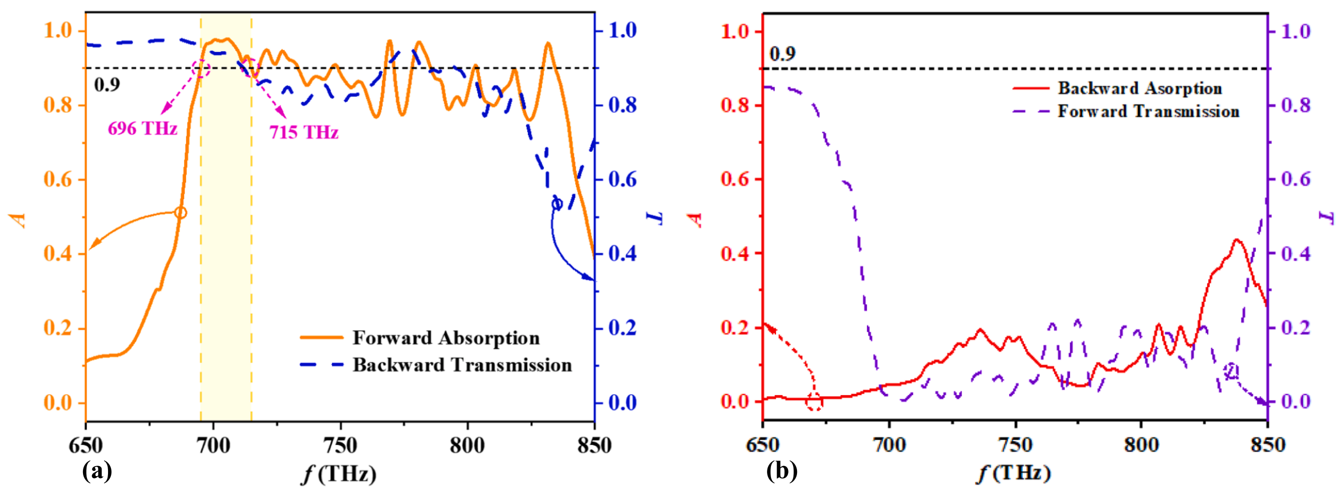

Fig. 3. For the TM modes, (a) forward absorption and backward transmission curves and (b) backward absorption and forward transmission curves of the SCMPC 1.

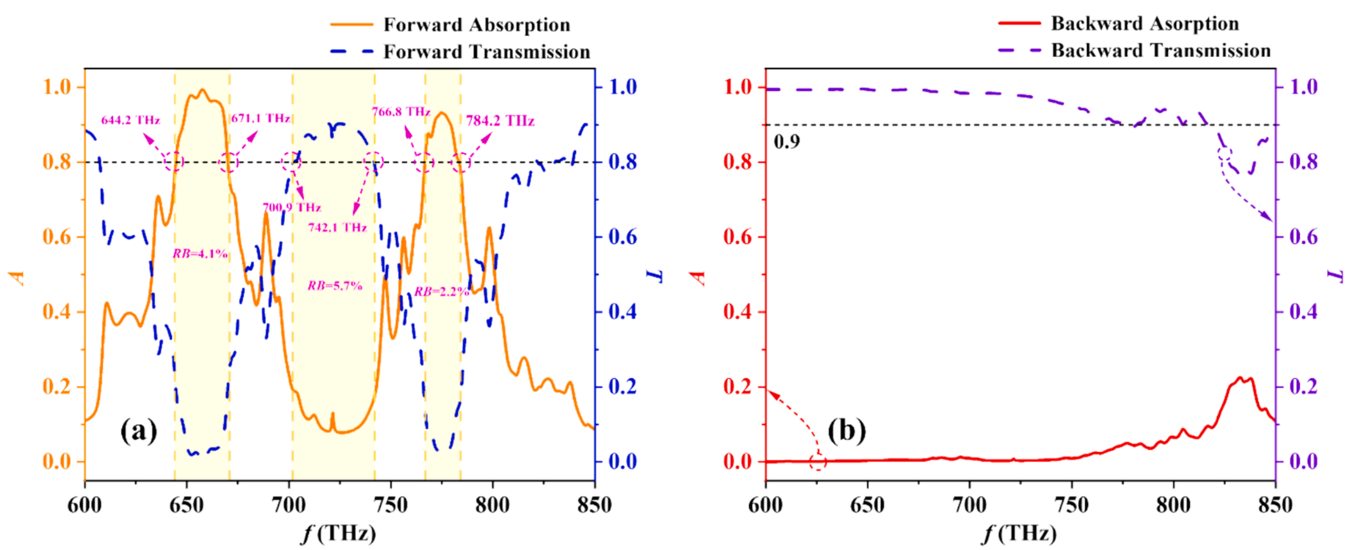

Fig. 4. (a) The absorption-transmission-absorption curves for the SCMPC 1 at forward incidence. (b) Propagation characteristics curves of the SCMPC1 at backward case.

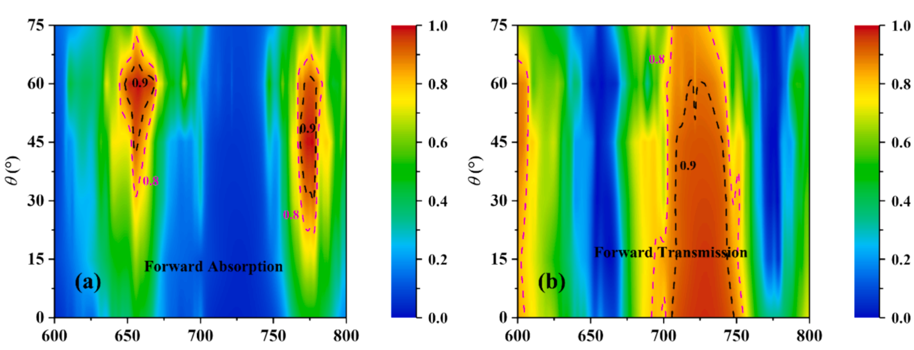

Fig. 5. Effects of variation of incident angle θ on (a) forward absorption, and (b) forward transmission of double-band rasorber phenomenon of the SCMPC 1.

perfect. The ideal result is 100 % absorption in one direction and 100 % transmission in the opposite direction [9]. Therefore, the SCMPC 2 is proposed to achieve broadband AAT. Similarly, based on the parameters mentioned earlier for the SCMPC 2, absorption for forward incidence and transmission for backward case are calculated when TM waves are incident in different directions and plotted in Fig. 7.

It is clear from Fig. 7 that the SCMPC 2 can achieve a continuous broadband AAT region with an *OB* of 428.3 ~ 670.5 THz and *RB* with absorption above 0.9 is 44.1 %. It is worth noting that in 428.3 ~ 670.5 THz, the transmission of plane EWs at backward incidence can reach

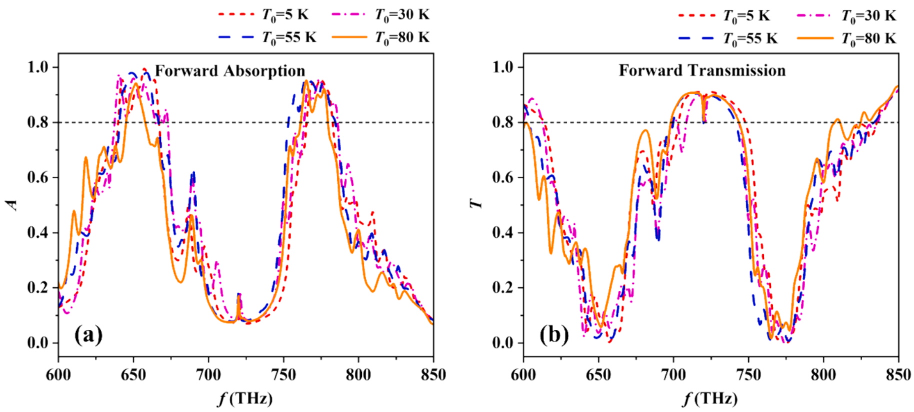

Fig. 6. Effects of different temperatures T_0 on (a) forward absorption, and (b) forward transmission of the double-band rasorber phenomenon of the SCMPC 1.

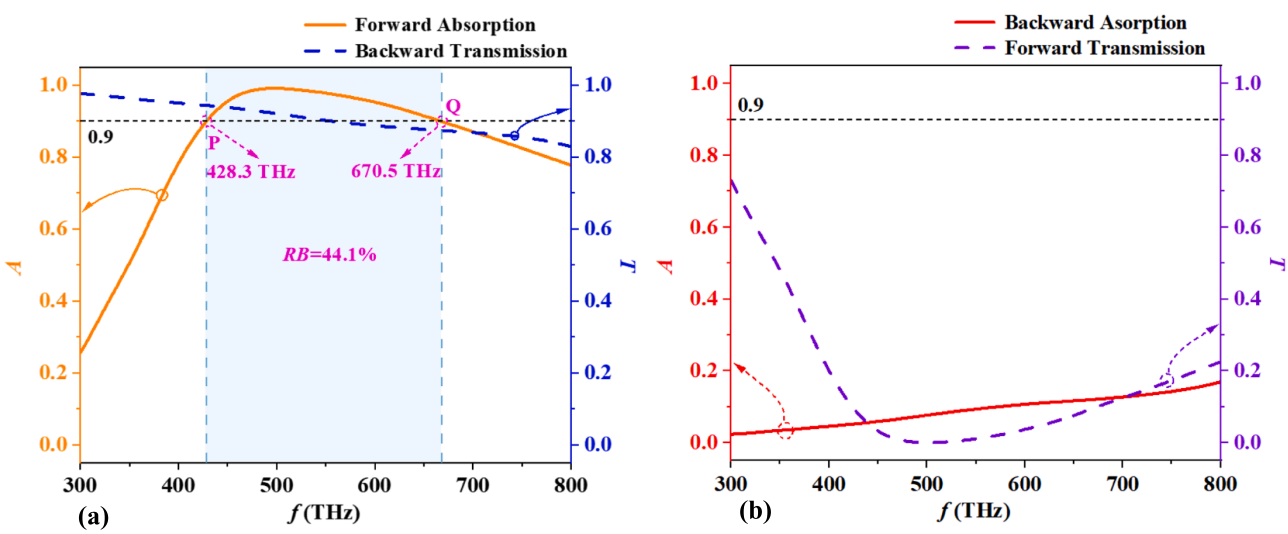

Fig. 7. (a) forward absorption and backward transmission curves and (b) backward absorption and forward transmission curves of the SCMPC 2 when T_0 = 50 K. Points P and Q indicate the intersection of absorption curves with A=0.9, and the broadband AAT region is indicated by the light blue shaded box.

0.88 or even higher, which means that total absorption for forward propagation and total transmission for backward propagation of EW can be perfectly realized. Due to better geometric asymmetry and higher structural complexity, Octonacci sequences are advantageous in achieving broadband AAT compared to ordinary periodic structures. In addition, it can be physically explained that the interaction between the incident EW and the irregularly arranged graphene layers causes an energy conversion that converts more electromagnetic energy into thermal energy, which leads to the realization of absorption resonance. Moreover, in SCMPC 2, the number of resonant cavities increases and mutual coupling occurs, which significantly broadens the absorption band.

In Fig. 8(a), we can figure out that for the forward propagation, the absorption phenomenon is not obvious when the incident angle θ is

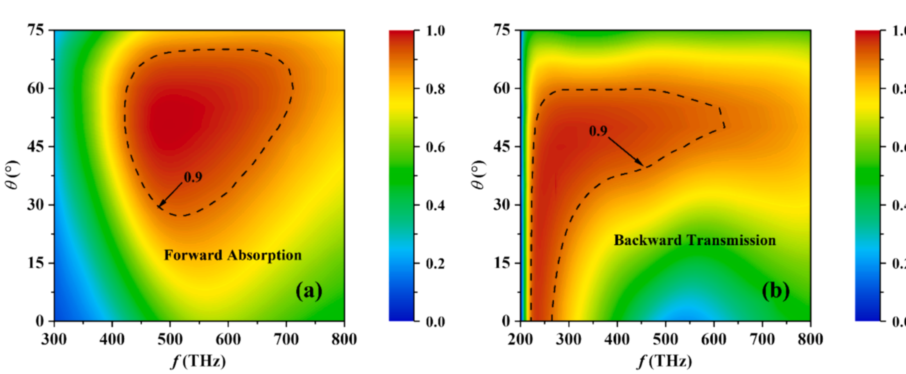

Fig. 8. Absorption and transmission spectra of the SCMPC 2 for different θ in both forward and backward propagation directions. (a) Absorption spectra in the forward propagation and (b) transmission spectra in the backward propagation. The ideal absorption and transmission regions are indicated by black dashed lines with a critical value of 0.9.

small. The range of high absorption ($A \geq 0.9$) gradually increases with the increase of θ, while the absorption properties show a tendency to deteriorate when θ is larger than 68°. Similarly, the transmission properties of backward propagation are shown in Fig. 8(b), and it is clear that the effective transmission area ($T \geq 0.9$) becomes significantly wider and shifts to the right at higher frequencies when θ becomes larger. However, once θ becomes larger than 60°, the transmission performance starts to deteriorate. Overall, the incident angle θ of EW plays a crucial role in modulating the propagation performance of the SCMPC 2, and a proper incidence direction is conducive to obtaining more significant broadband AAT properties.

In Fig. 9(a) and (b), it can be found that the effects of different ambient temperatures T_0 on absorption or transmission properties are not significant. When T_0 = 5 K, 30 K, 55 K, and 80 K, with an *OB* of 430 ~ 664 THz, *RB* with absorptivity higher than 0.9 is 42.7 %, which means that the broadband AAT of the SCMPC 2 exhibits good temperature stability.

As shown in Fig. 10(a)-(d), the thicknesses of metal and SC layers play a crucial role in the modulation of EW transmission characteristics. It can be seen that d_a has a significant effect on forward absorption and backward transmission. As d_a increases, both the absorption performance of forward propagation and the transmission performance of backward cases become worse. When d_a = 4 nm, *OB* is 428.3 ~ 670.5 THz and *RB* is 44.1 %, which has the most excellent broadband AAT performance at this time. When d_a = 12 nm, *OB* is 592.8 ~ 691.3 THz and *RB* is 15.3 %. In addition, absorption and transmission properties in both propagation directions are also affected by d_b. With d_b becoming thicker, the *RB* of forward absorption decreases, from 47.5 % at d_b = 8 nm to 40.1 % at d_b = 16 nm. However, Fig. 10(d) demonstrates that an increase in d_b leads to a significant increase in backward transmission. When d_b = 8 nm, the minimum backward transmittance value is 0.88 with an *OB* of 425.8 ~ 690.8 THz. As d_b increases to 16 nm with an *OB* of 433.6 ~ 650.8 THz, the minimum value of the corresponding backward transmittance decreases to 0.84. From Fig. 10(a)-(d), the optimal values for d_a and d_b are about 4 nm and 12 nm, respectively, which provide useful structural optimization suggestions for achieving better broadband AAT.

From Eq.(9), it is known that the transmission characteristics of EW are closely related to the inclination angle φ of the SCMPC 2. For the incident angle θ = 45°, the effects of different φ on forward absorption and backward transmission are calculated and the results are plotted in Fig. 11. As shown in Fig. 11(a), the forward absorption peak moves to lower frequencies as φ increases and *RB* shows a tendency to increase and then decrease. The corresponding *RB*s with absorption greater than 0.9 are 39.1 %, 45.7 %, and 27.8 % for φ = 20°, 30°, and 50°, respectively. In Fig. 11(b), it can be seen that the backward transmission also varies with φ. With the increase of φ, the backward transmittance goes from the lowest value of 0.62 at φ = 20° to 0.82 at φ = 30° to 0.8 at φ = 50°, which shows a tendency of increasing and then decreasing. As mentioned above, the AAT performance of EW can be changed by adjusting the φ of the SCMPC 2.

The effects of different stacking numbers *M* of quasi-periodic Octonacci sequences on the absorption and transmission properties of EW propagating in different directions are illustrated in Fig. 12(a) and (b). In Fig. 12(a), the increase of *M* contributes to the improvement of forward absorption to some extent, especially in higher frequencies. With *M*=3, the *RB* for forward absorption above 0.9 is 24.7 %, and as the SCMPC becomes more complex up to *M*=6, the *RB* is as high as 44.1 %. However, once *M* exceeds 6 layers, the backward transmission performance is no longer excellent, which hurts AAT. In addition, the total thickness of the structure becomes larger, which is detrimental to the subsequent fabrication process. Therefore, a larger stacking number taken in an appropriate range is important for achieving broadband AAT.

4. Conclusion

In summary, a novel kind of SCMPC is proposed by skillfully combining the advantages of SC, metastructures, and photonic crystals, which can realize the effective combination of asymmetry, broadband, and temperature stability. In the periodically aligned SCMPC 1, AAT can be achieved with an *OB* of 696 ~ 715 THz, and the forward absorptivity and backward transmittance are both greater than 0.9. Meanwhile, the double-band rasorber phenomenon is also found, with corresponding *RB*s of 4.1 %, 5.7 %, and 2.2 %, respectively. For the quasi-periodic Octonacci sequence-aligned SCMPC 2, *RB* is 44.1 %, which enables good broadband AAT. Temperature has no significant effect on the performance of both SCMPCs, which exhibit great temperature stability. Notably, this asymmetric propagation does not require any applied magnetic field and has unique applications in the design of asymmetric optical devices.

Funding

This work was supported by the Postgraduate Research & Practice Innovation Program of Jiangsu Province (Grant No. KYCX23_1004).

CRediT authorship contribution statement

Lei Lei: Writing – original draft, Validation, Investigation. **Bao-Fei Wan:** Writing – original draft, Visualization, Validation, Funding acquisition. **Si-Yuan Liao:** Visualization, Software, Resources, Data curation. **Hai-Feng Zhang:** Writing – review & editing, Supervision, Project administration, Conceptualization.

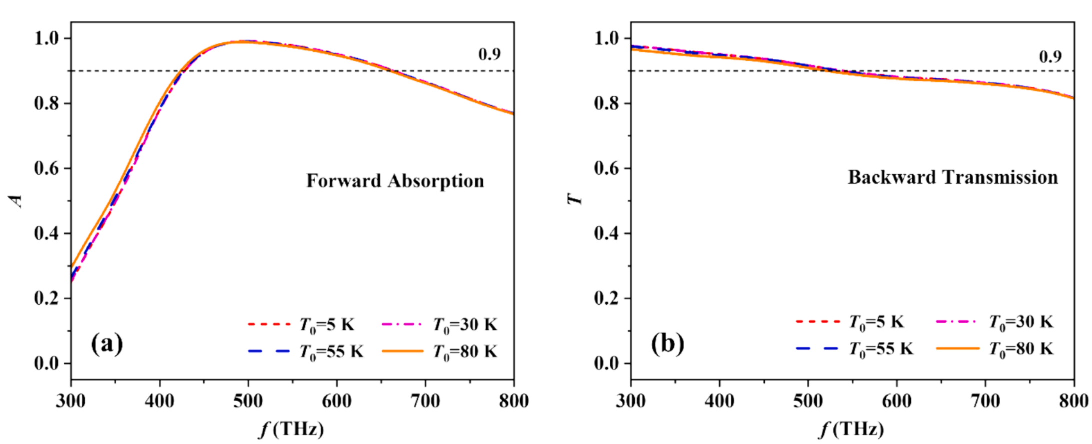

Fig. 9. Effects of different temperatures on (a) forward absorption, and (b) backward transmission.

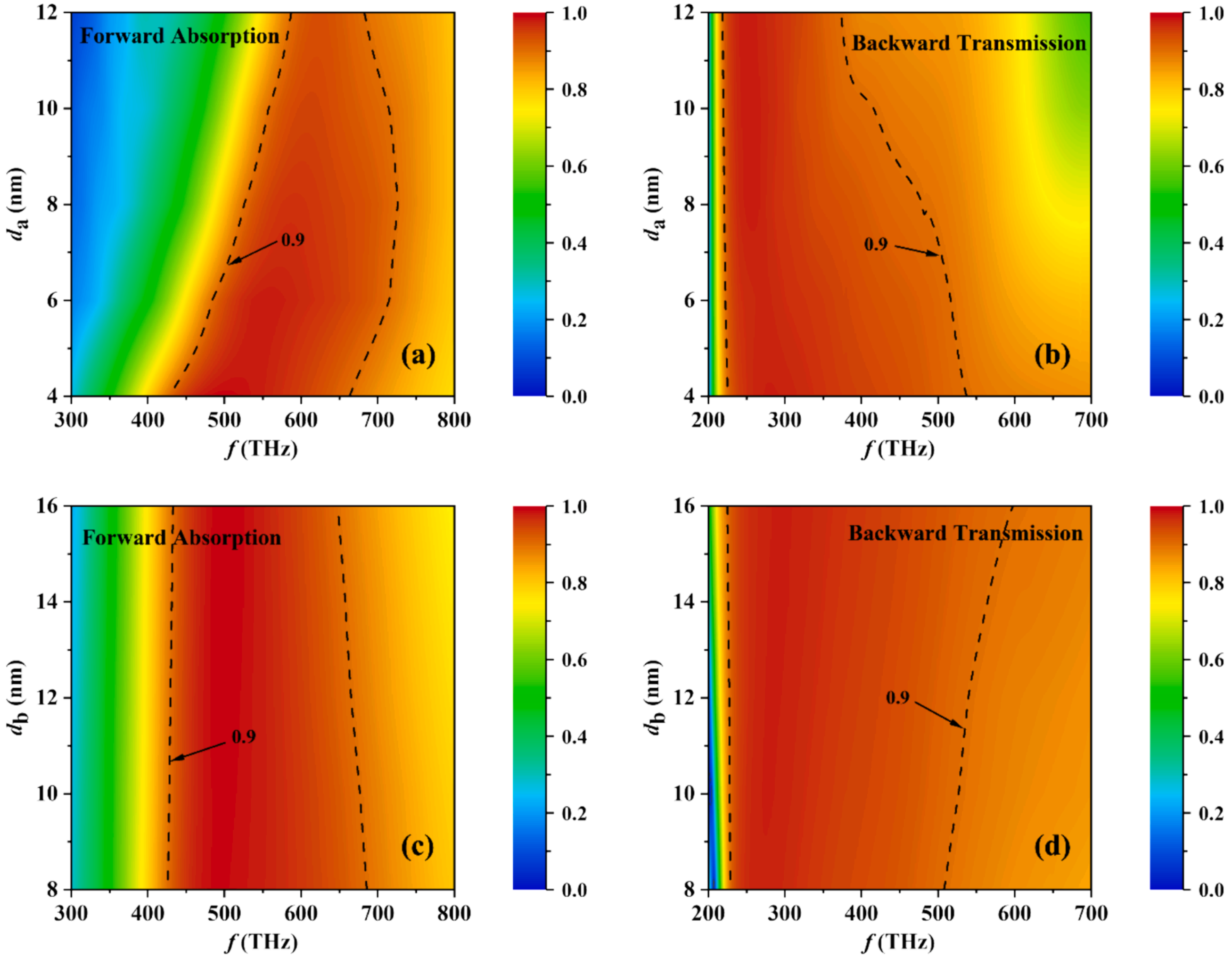

Fig. 10. The forward absorption and backward transmission properties of the SCMPC 2 about the thicknesses of the metal layer A and the SC layer B. Effects of d_a on (a) forward-propagating absorption spectra and (b) backward-propagating transmission spectra. Effects of d_b on (c) the forward-propagating absorption spectra and (d) the backward-propagating transmission spectra. The ideal absorption and transmission areas are indicated by black dashed lines with a critical value of 0.9.

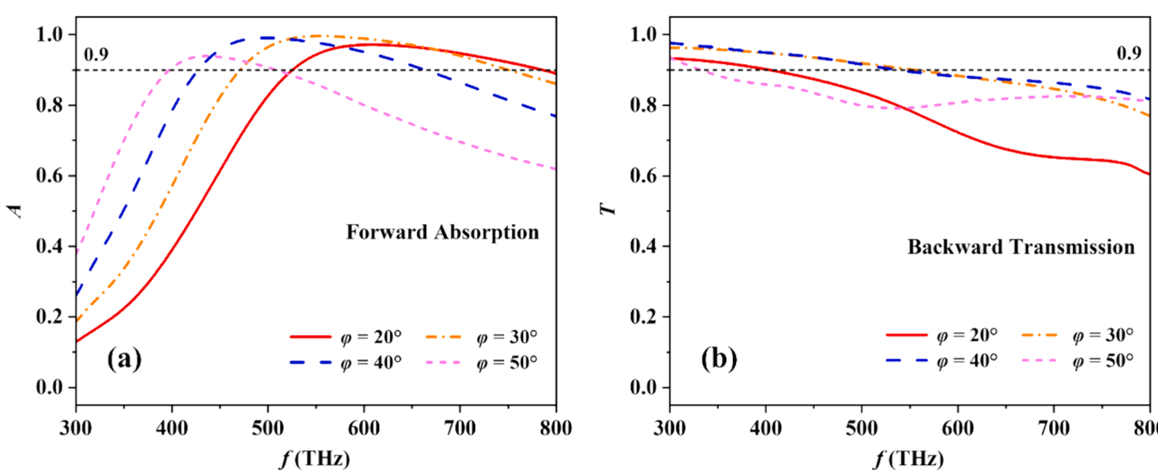

Fig. 11. Effects of the inclination angle φ on (a) forward absorption, and (b) backward transmission.

Declaration of Competing Interest

The authors declare that they have no known competing financial interests or personal relationships that could have appeared to influence the work reported in this paper.

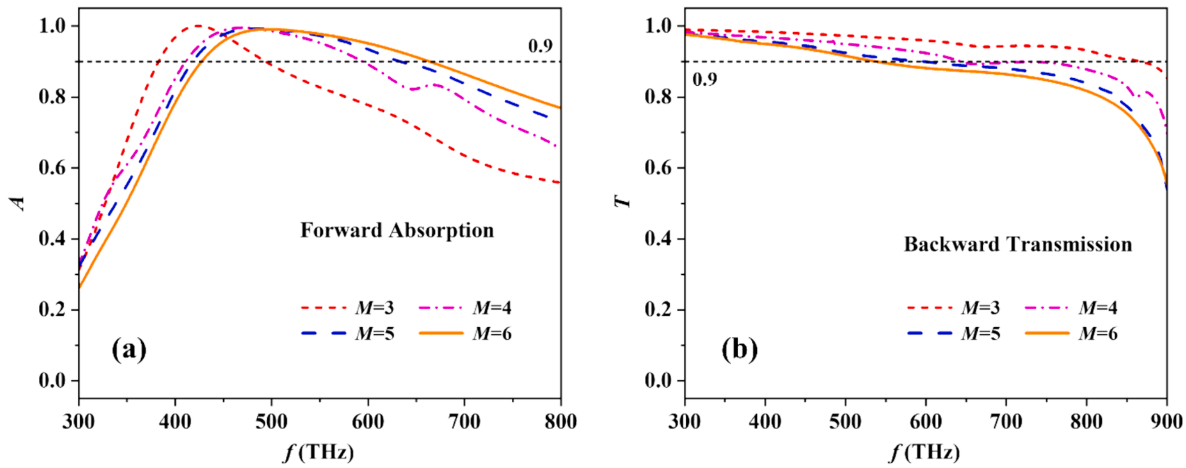

Fig. 12. Absorption and transmission curves in relation to stacking numbers *M* of the SCMPC 2. (a) Forward absorption curves as a function of *M*, and (b) the backward transmission curves as a function of *M*.

Appendix A. Supplementary data

Supplementary data to this article can be found online at https://doi.org/10.1016/j.jestch.2024.101810.

References

[1] S. Li, L.R. Huang, Y.H. Ling, W.B. Liu, C.F. Ba, H.H. Li, High-performance asymmetric optical transmission based on coupled complementary subwavelength gratings, Sci. Rep. 9 (2019) 17117.

[2] A.H. Gevorgyan, Reflection and transmission of light in medium/cholesteric/substrate and glass (1)/cholesteric/glass (2) systems, Tech. Phys. 45 (2000) 1170–1176.

[3] A.H. Gevorgyan, S.S. Golik, N.A. Vanyushkin, I.M. Efimov, Asymmetric absorption in asymmetric dielectric fabry-perot resonator with cholesteric liquid crystal layer inside, Opt. Mater. 125 (2022) 112111.

[4] B. Tang, Z. Li, Z. Liu, F. Callewaert, K. Aydin, Broadband asymmetric light transmission through tapered metallic gratings at visible frequencies, Sci. Rep. 6 (2016) 39166.

[5] L. Stephen, N. Yogesh, V. Subramanian, Broadband asymmetric transmission of linearly polarized electromagnetic waves based on chiral metamaterial, J. Appl. Phys. 123 (2018) 033103.

[6] T. Xu, H.J. Lezec, Visible-frequency asymmetric transmission devices incorporating a hyperbolic metamaterial, Nat. Commun. 5 (2014) 4141.

[7] J. Han, R. Chen, Dual-band metasurface for broadband asymmetric transmission with high efficiency, J. Appl. Phys. 130 (2021) 034503.

[8] D. Zhao, F. Fan, Z. Tan, H. Wang, S. Chang, Tunable on-chip terahertz isolator based on nonreciprocal transverse edge spin state of asymmetric magneto-plasmonic waveguide, Laser Photonics Rev. 17 (2023) 2200509.

[9] Y.T. Fang, Y.C. Zhang, Perfect nonreciprocal absorption based on metamaterial slab, Plasmonics 13 (2018) 661–667.

[10] M. Zarei, F. Nazari, M.K. Moravvej-Farshi, Tunable optical isolator using graphene-photonic crystal-based hybrid system, Phys. Scr. 96 (2021) 095502.

[11] J. Yuan, X. Kong, K. Chen, X. Shen, Q. Wang, C. Wu, Intelligent radome design with multilayer composites to realize asymmetric transmission of electromagnetic waves and energy isolation, IEEE Antennas Wirel. Propag. Lett. 19 (2020) 1511–1515.

[12] B. Han, S. Li, Z. Li, G. Huang, J. Tian, X. Cao, Asymmetric transmission for dual-circularly and linearly polarized waves based on a chiral metasurface, Opt. Express 29 (2021) 19643–19654.

[13] Y.F. Jiao, S.D. Zhang, Y.L. Zhang, A. Miranowicz, L.M. Kuang, H. Jing, Nonreciprocal optomechanical entanglement against backscattering losses, Phys. Rev. Lett. 125 (2020) 143605.

[14] D.E. Fernandes, M.G. Silveirinha, Asymmetric transmission and isolation in nonlinear devices: Why they are different, IEEE Antennas Wirel. Propag. Lett. 17 (2018) 1953–1957.

[15] V.S. Asadchy, M.S. Mirmoosa, A. Díaz-Rubio, S. Fan, S.A. Tretyakov, Tutorial on electromagnetic nonreciprocity and its origins, Proc. IEEE 108 (2020) 1684–1727.

[16] J.D. Adam, L.E. Davis, G.F. Dionne, E.F. Schloemann, S.N. Stitzer, Ferrite devices and materials, IEEE Trans. Microwave Theory Tech. 50 (2002) 721–737.

[17] A. Sheikh Ansari, A.K. Iyer, B. Gholipour, Asymmetric transmission in nanophotonics, Nanophotonics 12 (2023) 2639–2667.

[18] F. Fan, S. Chen, S.J. Chang, A review of magneto-optical microstructure devices at terahertz frequencies, IEEE J. Sel. Top. Quantum Electron. 23 (2017) 1–11.

[19] S.H.A. Bokhari, H.M. Cheema, Ultra-wideband, wide angle, asymmetric transmission based chiral metasurface for c and x band applications, Sci. Rep. 11 (2021) 11724.

[20] V.A. Fedotov, P.L. Mladyonov, S.L. Prosvirnin, A.V. Rogacheva, Y. Chen, N. I. Zheludev, Asymmetric propagation of electromagnetic waves through a planar chiral structure, Phys. Rev. Lett. 97 (2006) 167401.

[21] B. Khalichi, A. Ghobadi, A. Kalantari Osgouei, E. Ozbay, Diode like high-contrast asymmetric transmission of linearly polarized waves based on plasmon-tunneling effect coupling to electromagnetic radiation modes, J. Phys. d: Appl. Phys. 54 (2021) 365102.

[22] X. Tao, L. Qi, T. Fu, B. Wang, J.A. Uqaili, C. Lan, A tunable dual-band asymmetric transmission metasurface with strong circular dichroism in the terahertz communication band, Opt. Laser Technol. 150 (2022) 107932.

[23] A.H. Gevorgyan, Nonreciprocal waves in absorbing multilayer systems, Tech. Phys. Lett. 29 (2003) 819–823.

[24] K. Wang, S. Gao, Y. Wang, A. Nirmalathas, C. Lim, K. Alameh, E. Skafidas, Four-wave-mixing-based silicon integrated optical isolator with dynamic non-reciprocity, IEEE Photonics Technol. Lett. 28 (2016) 1739–1742.

[25] N.A. Vanyushkin, A.H. Gevorgyan, S.S. Golik, Scattering of a plane wave by an inhomogeneous 1d dielectric layer with gradient refractive index, Opt. Mater. 127 (2022) 112306.

[26] C.C. Chung, F.P. Lai, S.X. Huang, Y.S. Chen, Anisotropic metasurface with asymmetric propagation of electromagnetic waves and enhancements of antenna gain, IEEE Access 9 (2021) 90295–90305.

[27] H. Ye, J.F. Wei, L. Lin, F.C. Liu, L. Miao, S.W. Bie, J.J. Jiang, A frequency-selective surface rasorber based on four functional layers, IEEE Trans. Antennas Propag. 69 (2021) 2768–2778.

[28] Q.X. Guo, J.X. Su, Z.R. Li, J.M. Song, Y.L. Guan, Miniaturized-element frequency-selective rasorber design using characteristic modes analysis, IEEE Trans. Antennas Propag. 68 (2020) 6683–6694.

[29] Y.T. Jia, A.Q. Wu, Y. Liu, W.B. Zhang, Z.P. Zhou, Dual-polarization frequency-selective rasorber with independently controlled dual-band transmission response, IEEE Antennas Wirel. Propag. Lett. 19 (2020) 831–835.

[30] B. Wu, Y.J. Yang, H.L. Li, Y.T. Zhao, C. Fan, W.B. Lu, Low-loss dual-polarized frequency-selective rasorber with graphene-based planar resistor, IEEE Trans. Antennas Propag. 68 (2020) 7439–7446.

[31] S.R. Ovshinsky, R.T. Young, D.D. Allred, G. DeMaggio, G.A. Van der Leeden, Superconductivity at 155 K, Phys. Rev. Lett. 58 (1987) 2579–2581.

[32] D. van Delft, P. Kes, The discovery of superconductivity, Phys. Today 63 (2010) 38–43.

[33] P. Tassin, T. Koschny, M. Kafesaki, C.M. Soukoulis, A comparison of graphene, superconductors and metals as conductors for metamaterials and plasmonics, Nat. Photonics 6 (2012) 259–264.

[34] A.H. Aly, S.S.A. Ghany, B. Kamal, D. Vigneswaran, Theoretical studies of hybrid multifunctional $YaBa_2Cu_3O_7$ photonic crystals within visible and infra-red regions, Ceram. Int. 46 (2020) 365–369.

[35] S.K. Srivastava, Study of defect modes in 1D photonic crystal structure containing high and low T_C superconductor as a defect layer, J. Supercond. Novel Magn. 27 (2014) 101–114.

[36] A.H. Aly, D. Mohamed, The optical properties of metamaterial-superconductor photonic band gap with/without defect layer, J. Supercond. Novel Magn. 32 (2019) 1897–1902.

[37] Y. Trabelsi, N.B. Ali, M. Kanzari, Tunable narrowband optical filters using superconductor/dielectric generalized thue-morse photonic crystals, Microelectron. Eng. 213 (2019) 41–46.

[38] J. Chen, Y. Wang, B. Jia, T. Geng, X. Li, L. Feng, W. Qian, B. Liang, X. Zhang, M. Gu, S. Zhuang, Observation of the inverse doppler effect in negative-index materials at optical frequencies, Nat. Photonics 5 (2011) 239–242.

[39] D. Schurig, J.J. Mock, D.R. Smith, Electric-field-coupled resonators for negative permittivity metamaterials, Appl. Phys. Lett. 88 (2006) 041109.

[40] A. Alu, N. Engheta, Pairing an epsilon-negative slab with a mu-negative slab: Resonance, tunneling and transparency, IEEE Trans. Antennas Propag. 51 (2003) 2558–2571.
[41] C.J. Wu, C.L. Liu, T.J. Yang, Investigation of photonic band structure in a one-dimensional superconducting photonic crystal, J. Opt. Soc. Am. B 26 (2009) 2089–2094.
[42] A.H. Gevorgyan, A. Kocharian, G.A. Vardanyan, Accumulation and transmission of the light energy in nonreciprocal multilayer systems, Opt. Commun. 259 (2006) 455–464.
[43] V. Sepahvandi, B. Rezaei, A.H. Aly, Tunable multichannel fibonacci one-dimensional terahertz photonic crystal filter, Sci. Rep. 13 (2023) 5631.
[44] W. Jiang, J. Liu, T. Xia, N. Liu, Q.H. Liu, A necessary and sufficient condition for having independent TE and TM modes in an anisotropic waveguide, IEEE Trans. Microwave Theory Tech. 65 (2017) 3660–3670.
[45] B.F. Wan, H.N. Ye, H.F. Zhang, Ultra-wideband polarization insensitive angle filter based on ENZ characteristics and dynamic antireflection structures, Photonics 9 (2022) 110854.
[46] H.U. Yang, J. D'Archangel, M.L. Sundheimer, E. Tucker, G.D. Boreman, M. B. Raschke, Optical dielectric function of silver, Phys. Rev. B 91 (2015) 235137.
[47] B. Dominique, G. Thomas, Fitting the optical constants of gold, silver, chromium, titanium, and aluminum in the visible bandwidth, J. Nanophotonics 8 (2014) 083097.
[48] S.J. Guo, C.X. Hu, H.F. Zhang, Unidirectional ultrabroadband and wide-angle absorption in graphene-embedded photonic crystals with the cascading structure comprising the octonacci sequence, J. Opt. Soc. Am. B 37 (2020) 2678–2687.
[49] Z.B. Ye, P.H. Wu, H.L. Wang, S. Jiang, M. Huang, D.G. Lei, F. Wu, Multimode tunable terahertz absorber based on a quarter graphene disk structure, Results Phys. 48 (2023) 106420.